Optik 125 (2014) 5029–5035

Contents lists available at ScienceDirect

Optik

journal homepage: www.elsevier.de/ijleo

Phase diversity for calibrating noncommon path aberrations of adaptive optics system under nonideal measurement environment

Xinxue Ma[a], Jianli Wang[a], Bin Wang[a,*], Hongzhuang Li[a]

[a] Laboratory of Optoelectronic Detection, Changchun Institute of Optics, Fine Mechanics and Physics, Chinese Academy of Sciences, Changchun 130033, China

ARTICLE INFO

Article history:
Received 19 July 2013
Accepted 11 January 2014

Keywords:
Phase diversity
Aberration
Wavefront
Zernike
Estimation

OCIS codes:
wavefront sensing (010.7350)
adaptive optics (010.1080)
telescopes (110.6770

ABSTRACT

When the defocus cannot be measured and the wavefront solution set is restricted by a multi-channel, some practical problems exist in the calibration of the noncommon path aberrations of the adaptive optics system. To solve these problems, an evaluation function of phase diversity algorithm is constructed in this paper. We use the method that the estimated aberration and the modulated deformable mirror iterate each other to make up the nonideal measurement environment. Then the ill-pose problem of the solution by phase diversity, produced as relaxing constraints of the diversity defocus on the wavefront solution set, is solved. We have adopted the proposed method to measure the noncommon path aberrations of the adaptive optics system on a 1.23 m telescope. Experimental results demonstrate that wavefront solution is more accurate and the whole imaging quality is improved effectively by using the deformable mirror to compensate the aberration measured.

1. Introduction

In the optical system, one optical path is divided into two beams: one estimates the system wavefront phase, the other gets into the terminal imaging camera. To ensure the exact match between the wavefront correction effects and the camera imaging results, the wavefront phase difference between the two beams from the optical path should be minimized. For the optical path adjustment (components, processing, etc.), there are noncommon path aberrations between the two beams, which affects the correction effect. If the noncommon path aberrations are measured accurately and the deformation mirror as the initial surface shape is added, it will improve the correction effect and system imaging quality significantly. However, the measurement of the noncommon path aberrations is under the precondition of the maintenance of the optical system path, and the traditional testing equipment cannot be used.

The phase diversity (PD) technique, proposed by Gonsalves, extracts phase information from focused and defocused images and recovers the object with known defocus [1]. The PD technique not only simplifies the optical path of wavefront and complexity, but also estimates the extended object and gets rid of the dependence on the point object for the majority of wavefront sensors [2]. The PD theory had been further perfected by Paxman et al. [3–5], and the mathematical model of the multi-frame PD under Gaussian noise and Poisson noise was given, where the estimated precision of PD with noise is improved greatly. Vogel et al. proposed the fast numerical solution using the theories of inverse problem [6,7]. Löfdahl et al. had applied the phase-diverse speckle (PDS) theory to the field of solar observation successfully, and high imaging resolution is obtained for the solar surface structure [8,9].

In the field of optical estimation, PD is used to estimate the aberration, alignment errors, mirror flatness etc. Bolcar introduced PD theory into the estimation of synthetic aperture and segmented mirror [10,11]. Löfdahl et al. applied phase-diverse phase retrieval (PDPR) to calibrate the noncommon path aberrations of the AO system on KECK telescope. Mugnier and Blanc et al. proposed the edge of estimation PD theory, applied PD technology to the imaging restoration of French NAOS-CONICA astronomical telescope and calibrated the static aberration of AO system [12–14].

In this paper, we designed a system to calibrate the noncommon path aberrations of a 137 unit AO system on a 1.23 m telescope when the defocus cannot be measured. We constructed an evaluation function of phase diversity (PD), restricted the wavefront

* Corresponding author.
E-mail address: eatingbeen@hotmail.com (B. Wang).

http://dx.doi.org/10.1016/j.ijleo.2014.01.129
0030-4026/

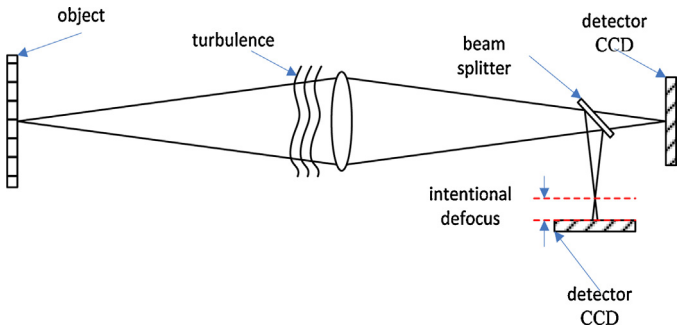

Fig. 1. Scheme of data-collection image by PD.

solution set by a multi-channel, and used the method to iterate the estimated aberration and the modulated deformable mirror with each other to make up the nonideal measurement conditions, we got more accurate wavefront solution by PD where the constraints of diversity defocus on the wavefront solution set relaxed. We enhanced the telescope imaging quality effectively by using the initial bias of the deformable mirror to compensate the aberration measured.

The remainder of this paper is organized as follows: Section 2 describes the basic theory of PD and the definition of variable; Section 3 describes the overall experiment; Section 4 gives the experimental results and discussion; the conclusion is given in Section 5.

2. Theory

As the point-spread function (PSF) can be mapped to multiple wavefronts, the wavefront solution from a single image are ill-posed.

Comparing to a single channel which takes the wavefront as unknown to resolve the blind deconvolution, PD uses PSFs of images collected by two channels to restrict the wavefront, where a fixed amount of defocus are known. Therefore, the ill-pose problem [15–20] is reduced in the wavefront solution.

The optical path of the PD system, with focus and defocus collection channels, is illustrated in Fig. 1. Based on the engineering necessity, the numbers of collection channels can be increased. The problem of PD imaging restoration can be regarded as the inverse problem of seeking the original signal phase [21,22] through the known analog of the interference signal or an adaptive filter.

2.1. Imaging system model

The atmosphere and telescope can be approximately regarded as a linear space-invariant system. In the non-coherent light illumination, the imaging function with Gaussian noise is defined as [1]

$$d(x) = f(x) * s(x) + n(x), \tag{1}$$

where d is the real estimated image; f is the ideal object image; s is the PSF; n is the Gaussian noise; x is the coordinates of image plane; and* denotes a convolution. The intensity PSF is defined as [1]

$$s(x) = \left| \mathcal{F}^{-1} \left\{ P(\upsilon) e^{i\phi(\upsilon)} \right\} \right|^2, \tag{2}$$

where $\mathcal{F}^{-1}$ is the inverse Fourier transform operator; υ is the complex plane coordinate; P is the pupil function; and φ is the wavefront phase, which can be decomposed into a set of Zernike polynomials:

$$\phi(\upsilon) = \theta(\upsilon) + \sum_{m=1}^{M} \alpha_m Z_m(\upsilon), \tag{3}$$

where α_m is the mth coefficient of polynomials; Z_m is the mth basis Zernike polynomial; and θ is the known fixed-defocus phase.

2.2. Evaluation function

The mathematical model of PD can be understood as an adaptive filter. In the Gaussian noise model, the mean square deviation of the object and multi-channel images can be used as likelihood function. In frequency domain, the evaluation function of the multi-channel PD mentioned is defined as

$$L(f, \alpha) = \frac{1}{2N} \sum_u \left(\sum_{c=1}^{C} \sigma_c^{-2} \left| D_c(u) - FS_c(u) \right|^2 + \gamma \left| F(u) \right|^2 \right), \tag{4}$$

where u is spatial-frequency domain coordinate; C is the number of channels; N is the total number of pixels of a single image; α and f are the unknown phase and object parameters, respectively; D_c, F, and S_c are the Fourier transformation of d_c, f and s_c, respectively; The second term in the right pair of brackets is the Tikhonov regularization term, used to improve the numerical stability and speedup the convergence of the algorithm [6,7]; γ is the regular coefficient, which is non-negative; and σ_c^{-2} (σ is non-negative) is the reciprocal of the noise variance in channel c.

The stationary point F expressed in Eq. (5) can be obtained by setting the derivative Eq. (4) to F to be 0. Eq. (6) is obtained by substituting Eq. (5) into Eq. (4). Thus, we can use the target state estimator as an independent intermediate process separated from the phase estimator, and then get an evaluation function which is independent of the object [4]. The expression of the target state estimator is the intermediate process of deriving the evaluation function. It has the same form as the wiener filter and reduces the influence of noise effectively.

$$F = \frac{\sum_{c=1}^{C} \sigma_c^{-2} D_c S_c^*}{\gamma + \sum_{c=1}^{C} \sigma_c^{-2} \left| S_c \right|^2}, \tag{5}$$

$$L(\alpha) = \frac{1}{2N} \sum_u \left(\sum_{c=1}^{C} \sigma_c^{-2} \left| D_c \right|^2 - \frac{\left| \sum_{c=1}^{C} \sigma_c^{-2} D_c S_c^* \right|^2}{\gamma + \sum_{c=1}^{C} \sigma_c^{-2} \left| S_c \right|^2} \right). \tag{6}$$

Eq. (6) is the evaluation function, when the readout noise is inconsistent among the multi-channel. The multi-channel is realized by collecting images at focus plane; and some defocus is known through changing the position of imaging camera by the focusing motor. So σ_c^{-2} has the same value in all channels. The value of σ_c^{-2} can be obtained from collecting the background noise of the camera when the photon noise is ignored.

After the determination of the evaluation function, the process of the wavefront estimation and image restoration can be described as a mathematical optimization problem, which is, a large scale optimization problem. In this paper, we solve the optimization problem by using the quasi-Newtonian method, where the inverse Hessian approximation is used to mimic the property of the true inverse Hessian matrix. And the inverse Hessian approximation is updated using the L-BFGS-B formula [23–28].

3. Experiment

In this section we discuss the relevant details of the experiment. Section 3.1 describes the system components; Section 3.2 describes the experimental procedure; Section 3.3 gives the analysis and solution of the main problems.

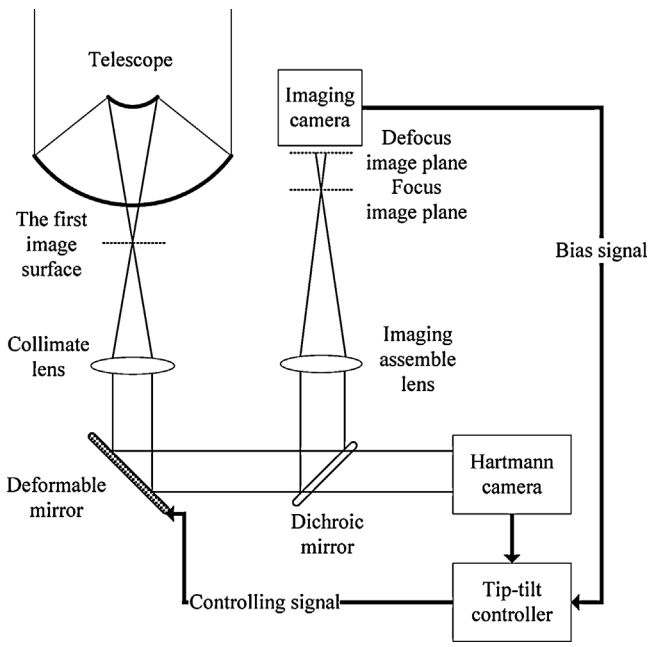

Fig. 2. Schematic of experimental system.

3.1. System components

We designed a system to calibrate the noncommon path aberrations based on the AO system on a 1.23 m telescope. The theory of the system is shown in Fig. 2. The light beam from the telescope is collected on the first image plan through collimating lens, then becomes parallel, and is injected into DM. After shaped by DM, the beam refracts onto the dichroic mirror and then is divided into two: one gets into the scientific CCD through the imaging lens, called the imaging path, the other enters into the 11×11 Hartmann wavefront sensors (HWS), called the AO path. The optical path before dichroic mirror is called the common path. The wavefront sensor estimates the wavefront of the common and AO paths rather than that of the common and image paths, which affects the imaging quality on the imaging camera. The difference between these two paths causes the static aberration called the noncommon path aberrations. The motivation for this experiment is to quantitatively measure the static aberration from the first image to the focal plane of imaging path and improve the overall imaging quality of the AO system by pre-compensating the static aberration.

3.2. Experimental procedure

Step 1: Close the main mirror cover and put a white optical-fiber source on the first imaging plane through the light box inside the device as displayed in Fig. 2.

Step 2: Calibrate the DM; closed-loop control the DM according to the measured wavefront by the HWS, and try to compensate the aberration from the first imaging plane to the HWS.

Step 3: Move the imaging camera to the focal plane; set the exposure time of the camera to ensure that the grey value of images would not be saturate; and collect images.

Step 4: Move the imaging camera and collect images. If C defocus channels are used to seek the wavefront solution set, these process should be repeated C times.

Step 5: Close the optical-fiber source, and collect the background of the camera to count the readout noise of the camera.

Step 6: Input the collection images and defocus amounts to a PD program to acquire the static aberration and the recovered images.

Step 7: Make precompensation of the static aberration calculated by the PD program to improve the imaging quality.

3.3. Analysis and solution of main problems

A series of problems will be encountered when the noncommon path aberrations are estimated without changing the optical path of the AO system.

First, there is no encoder or other readout device above on the focusing platform. As a result, the defocus of the imaging camera cannot be measured accurately.

Second, it is hard to increase the whole system focal length since the secondary imaging procedure will work as a magnification process for the image corresponding to the first image plane of the large-diameter telescope system. The focal length of the collimating lens, the focal length of the imaging lens and the image magnification for the first image plane are assumed to be f_1, f_2 and $K = f_2/f_1 = 4.4$, respectively. We have fiber-optics splice with diameter equal to 25 μm. The pixel dimension of the imaging camera is 13 μm, when it is put on the first image plane; the ideal image diameter is 8.5 pixels, it is not an ideal point source. In sum, the problem is on how to improve the ill-pose problem of the wavefront solution by PD.

Third, the transitional axis of the focus motor and the optical axis are not parallel.

Fourth, the solution precision is related to the estimated wavefront aberration. The smaller the amplitude is, the higher the solution precision is. At the initial stage of the alignment, the aberration is relative big, so it affects the measurement precision by PD.

Determining how to improve the tolerance of the algorithm under such experimental conditions in a practical project will be critical of the PD in the noncommon path aberrations measurement applications. We propose the following improvements to solve the above problems.

The solution to the first problem is the shifting that satisfies the normal distribution in the case of the focusing motor at every step: $N(l, \sigma_l^2)$. The defocus we need is Z_c for a channel C, the actual defocus is $z_c \sim N\left(Z_c, Z_c/l\sigma_l^2\right)$, the focusing error is $\Delta_c = z_c - Z_c \sim N\left(0, \left(Z_c/l\right)\sigma_l^2\right)$, the wavefront error caused by focusing error is $\theta_{\Delta c}(r) = \left(\pi \times \Delta_c \times r^2\right) / \left(4\lambda(F\#)^2\right)$ $(r \in [0, 1])$, where r is the radial coordinate on the unit circle. When the adjustment errors of defocus exist in every defocused channel, Eq. (3) changes into:

$$\phi_c(\upsilon) = \theta_c(\upsilon) + \theta_{\Delta c}(\upsilon) + 2\pi \sum_{m=1}^{M} \alpha_m Z_m(\upsilon). \tag{7}$$

Using a joint maximum likelihood (ML) approach, an estimator can be defined as

$$\left(\left\{\hat{\alpha}\right\}, \left\{\Delta\right\}, \hat{f}\right)_{\mathrm{ML}} = \underset{\{\alpha\},\{\Delta\},\mathbf{f}}{\operatorname{argmax}} \Pr\left[\left\{\mathbf{d}\right\}; \{\alpha\}, \left\{\Delta\right\}, \mathbf{f}\right], \tag{8}$$

the relationship of $\Delta_1, \Delta_2, \ldots, \Delta_C$ is correlative, we assume that those are independent to make formula simplify.

$$\begin{aligned} Pr\left[\left\{\mathbf{d}\right\}; \{\alpha\}, \left\{\Delta\right\}, \mathbf{f}\right] &= \prod_{c=1}^{C}\prod_{x \in \chi} Pr\left[\mathbf{d}_c(x); \{\alpha\}, \Delta_c, \mathbf{f}\right] \\ &= \prod_{c=1}^{C}\prod_{x \in \chi} Pr\left[\mathbf{d}_c(x) \mid \{\alpha\}, \Delta_c, \mathbf{f}\right] Pr\left[\{\alpha\}, \Delta_c, \mathbf{f}\right] \\ &= \prod_{c=1}^{C}\prod_{x \in \chi} Pr\left[\mathbf{d}_c(x) \mid \{\alpha\}, \Delta_c, \mathbf{f}\right] Pr\left[\Delta_c \mid \{\alpha\}, \mathbf{f}\right] Pr\left[\{\alpha\}, \mathbf{f}\right] \end{aligned} \tag{9}$$

For the estimation problem, $\Pr[\{\alpha\}, \mathbf{f}] = 1$ and $\Pr[\Delta_c | \{\alpha\}, \mathbf{f}] = \Pr[\Delta_c]$, so we have

$$\left[\left\{\mathbf{d}\right\}; \{\alpha\}, \left\{\Delta\right\}, \mathbf{f}\right] = \prod_{c=1}^{C}\prod_{x\in\chi} Pr\left[\mathbf{d}_c(x) | \{\alpha\}, \Delta_c, \mathbf{f}\right] Pr\left[\Delta_c\right], \quad (10)$$

where

$$Pr\left[\mathbf{d}_c(x) | \{\alpha\}, \Delta_c, \mathbf{f}\right] = \frac{1}{\sqrt{2\pi\sigma_c^2}} \exp\left\{-\frac{\left[\mathbf{d}_c(x) - f * s_c(x)\right]^2}{2\sigma_c^2}\right\}, \quad (11)$$

$$\Pr\left[\Delta_c\right] = \frac{1}{\sqrt{2\pi Z_c \sigma_l^2 / l}} \exp\left\{-\frac{\Delta_c^2}{2 Z_c \sigma_l^2 / l}\right\}. \quad (12)$$

We take Eqs. (11) and (12) into Eq. (10), ignore the constant term, then we get

$$L\left(\{\alpha\}, \left\{\Delta\right\}, \mathbf{f}\right) = \sum_{c=1}^{C} \frac{1}{2\sigma_c^2} \left\|\mathbf{d}_c - \mathbf{f} * \mathbf{s}_c\right\|^2 + \frac{Nl}{2\sigma_l^2} \sum_{c=1}^{C} \frac{\Delta_c^2}{Z_c} \quad (13)$$

We can see that in the condition of the unknown actual focus, the objective function of PD is $Nl/2\sigma_l^2 \sum_{c=1}^{C} \Delta_c^2 / Z_c$. The stable point is invariant after joining the objective function on F. Thus, we omit the intermediate process, and then get the reconstructive objective function:

$$L(\{\alpha\}, \left\{\Delta\right\}) = \frac{1}{2N} \sum_{u} \left(\sum_{c=1}^{C} \sigma_c^{-2} \left|D_c\right|^2 - \frac{\left|\sum_{c=1}^{C} \sigma_c^{-2} D_c S_c^*\right|^2}{\gamma + \sum_{c=1}^{C} \sigma_c^{-2} \left|S_c\right|^2} \right) + K \frac{Nl}{2\sigma_l^2} \sum_{c=1}^{C} \frac{\Delta_c^2}{Z_c}, \quad (14)$$

where K is a constant used to adjust the focusing errors in the proportion of the object function. We solve the wavefront expression with Eq. (7).

It is worth noting that Eq. (14) as the objective function of PD relaxes the constraints of the defocus diversity on the solution set of the wavefront, to some extent, which will increase the ill-pose problem of the solution by PD to some extent. It is really a prerequisite when you cannot accurately measure the defocus of the focus channel. The solid line represents Eq. (6), which is, the objective function monitors the consistency of the noisy data across all the channels relative to the forward model estimates. Since there is a deviation between the actual focus of channel 2 and the prospective focus, it makes the phase defocus diversity solution by the constrained wavefront wrong. Thus, a wrong constraint causes a wrong wavefront solution. The dotted line represents Eq. (14) as the objective function of the wavefront solution set obtained by two channels. In fact, Eq. (14) as the objective function of PD is certain to relax the constraints of the defocus diversity on the wavefront solution set, which makes the solution set of each channel increase appropriately. Therefore, the true wavefront solution will fall into the intersection of the solutions sets corresponding to wavefront 1 and 2.

The solution of the first problem increases the ill-pose problem of the solution by PD, so we will combine the remainder of the first and second problems to weak the ill-pose of the PD solution.

The most direct method to solve this problem is just to increase the number of channels, which are used one group images measured on the focal plane and several groups images measured in different defocus as the inputs of PD program. Thus, the ill-pose of the wavefront solution set by PD will be improved. The wavefront solution set calculated by searching algorithm is more approximate to the real wavefront when it is subjected to the multi-channel data.

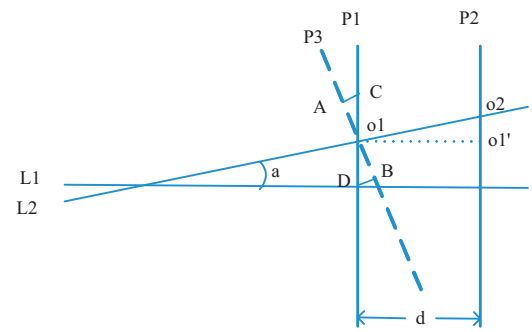

Fig. 3. Relational graph between ray axis and motor transmission shaft of focusing.

It would be well to collect the multi-channel data at the same moment. But our system can only collect datum at a different moment by controlling the focus motor. So it is required that the shape of the fiber-optics splice object does not change in the process of collection. As the estimated wavefront is a static optical aberration and does not change severely, the above conditions can be satisfied basically.

The solution of the third problem is illustrated in Fig. 3 $L1$ is the transitional axis of focus motor, $L2$ is optical axis, a is the included angle of $L1$ and $L2$, $P1$ is the focal plane of CCD along $L1$, $P2$ is the defocus plane and d is the distance between $P1$ and $P2$, $o1$ is the center of the image on $P1$, $o2$ is the center of the image on $P2$, $o1'$ is the projection of $o1$ on $P2$, $P3$ is an ideal focal plane and it is perpendicular to $L2$, the foot is $o1$. The included angle of $P3$ and $P1$ is a, AB is the width of the fiber-optics splice image on $P3$, CD is the width of the image on $P1$.

As shown in Fig. 3, $L1$ and $L2$ are not parallel, and the effects upon collecting datum of PD are mainly from the errors of the defocus and the anisoplanatism imaging.

The real defocus of two images collected at $P1$ and $P2$ by the imaging camera is $o1o2$, the moving distance of focus motor is d. If we take d as the input defocus into PD algorithm, there would be an error whose value is $o1o2 - d$. If we know a, we can eliminate the errors and get $o1o2 = d/\cos a$, and then make $o1o2$ as the input defocus into the PD algorithm. The value of a can be obtained through calculating images undershoot $o2o1'$ on $P1$ and $P2$, and the moving distance of the focus motor d as $a = \arctan(o2o1'/d)$. The problem of the anisoplanatism imaging can be ignored in our system, because $F\#$ reaching the imaging camera is about 40 and the system has satisfied the properties of linear optical system greatly. Thus, the wavefront of point A and B on the ideal focal plane $P3$ are consistent at the same time. But on the real focal plane $P1$, the terminals of the fiber-optics splice in the image are point C and D, and the wavefront of C and D are unequal. The defocus aberration is the primary, which is $\left(2\pi \times AB \times \tan\ a/(8 \times F\#^2 \times \lambda\right)$, the unit is λ, take $AB = 25 \times 10^{-6} \times 4.4$, $F\# = 40$ and $\lambda = 800 \times 10^{-9}$ into the above formula, the aberration is $(0.0675 \times \tan a)\lambda$. Assuming that $a = 30$rad, the aberration is just $5.89 \times 10^{-4}\lambda$. So we can ignore the problem of the anisoplanatism imaging caused by nonparallel between $L1$ and $L2$.

The solution of the last problem is assuming that the residual errors of the noncommon path can be compensated by DM. In general, the root mean square of the noncommon path aberrations within 0.3 will be feasible after considering the journey of DM. In order to calculate the noncommon path aberrations more precisely, we can operate in the way shown in Fig. 4. First, calibrate DM and use closed-loop control DM according to the wavefront estimated by the HWS to compensate the aberration from the first imaging plane to the HWS. Then estimate the aberration from the first

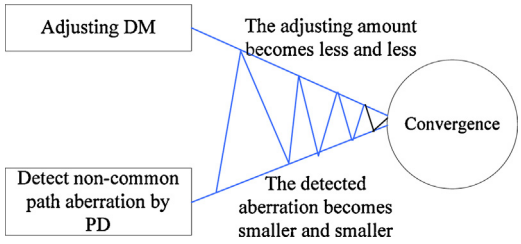

Fig. 4. The iterative repetition convergence between estimation by PD and adjusting by DM.

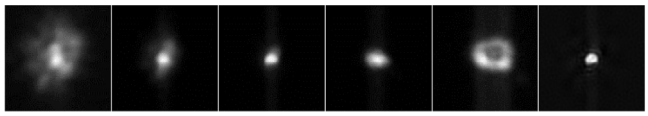

(a) Original images and results at the first time

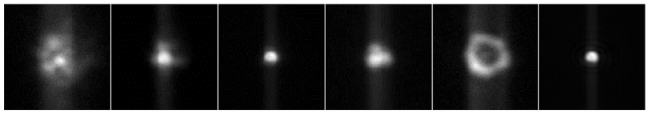

(b) Original images and results at the second time

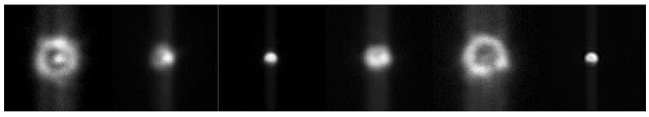

(c)Original images and retrieval at the third time

Fig. 5. The collection images of three exposures.

imaging plane to the imaging camera by multi-channel PD. As the aberration from the first imaging plane to the HWS has already been compensated, the aberration estimated by the multi-channel PD is the noncommon path aberrations. Then take the estimated aberration obtained by PD as the initial bias to adjust the DM. Repeating this procedure, both the noncommon path aberrations estimated by PD and the adjusting range of DM became smaller after carrying out each time, and finally convergent. In practical application, two or three iterations can achieve the convergence.

4. Results and discussion

F# between the experiment system and the imaging camera is 40, and the *F#* of the collimating lens is 9.1. The central wavelength is 800 nm and the focal depth is about 2.56 mm. In the experiment, we used five channels to help us construct an evaluation function of phase diversity (PD) processing when the defocus cannot be measured. We used the multi-channel to compensate for the sequelae brought by modifying the evaluation function. The corresponding defocuses are 0 mm, ±10 mm and ±20 mm. The pixel dimension of the imaging camera is 13 μm and the exposure time is 1ms. The source is the GCI-06 direct-current voltage regulation optical-fiber source and the lamp is a 150 W quartz-halogen lamp. The diameter of the fiber-optics splice object is 25 μm.

Table 1
Measurement results.

Zernike coefficients	Result 1	Result 2	Result 3
Astigmatism *Y*	−0.04126	0.02119	−1.17E − 05
Astigmatism *X*	0.07427	0.01356	0.01623
Coma *Y*	0.03320	−0.01572	0.00267
Coma *X*	−0.02844	0.02730	0.01050
Trefoil *Y*	0.00737	−0.02682	0.00652
Trefoil *X*	0.00917	−0.02414	−0.00813
Spherical	−0.07451	0.00728	−0.01821
Secondary astigmatism *Y*	−0.00736	0.00023	−0.00376
Secondary astigmatism *X*	−0.00041	−0.01828	−0.00236
Tetrafoil *Y*	0.00886	−0.00141	0.00045
Tetrafoil *X*	0.00095	0.01035	−0.00669

At the first time, we calibrate DM, then closed-loop control DM according to the wavefront estimated by the HWS to compensate the aberration from the first imaging plane to the HWS. At the second time, we take the Zernike coefficients into the control of DM to produce an initial bias, and repeat the collection process. The collection images of three exposures are illustrated in Fig. 5. The defocus of the images from left to right and then up to down is −20 mm, −10 mm, 0 mm, 10 mm and 20 mm. The last image is the restoration image from the fifth images above.

In this experiment, we take from the fifth to fifteen Zernike coefficients as unknown to search, because the first four items all need not be precompensated by DM. The piston is constant, which can be neglected. Two tilts can be precompensated by tip–tilt, and defocus can be precompensated by the focusing camera brought by modifying the evaluation function. We do not search higher-order aberrations, because the DM is an assembly of the experimental equipment, thus, the capability of correcting higher-order aberrations is relatively weak. The corresponding estimated wavefronts are illustrated in Fig. 6. MTF of the optical path between the first image planes to the CCD as shown in Fig. 7.

The imaging quality has been improved from the focus images of three times, and the full width at half maximum (FWHM) as illustrated in Fig. 8.

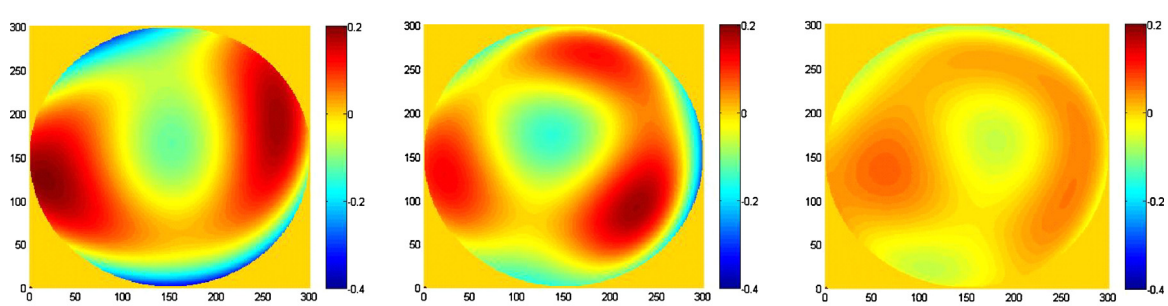

(a)The estimated wavefront at the first time, RMS = 0.129λ, PV = 0.798λ.

(b) The estimated wavefront at the second time, RMS = 0.083λ, PV = 0.491λ.

(c) The estimated wavefront at the third time, RMS = 0.0336λ, PV= 0.1706λ

Fig. 6. The corresponding estimated wavefronts.

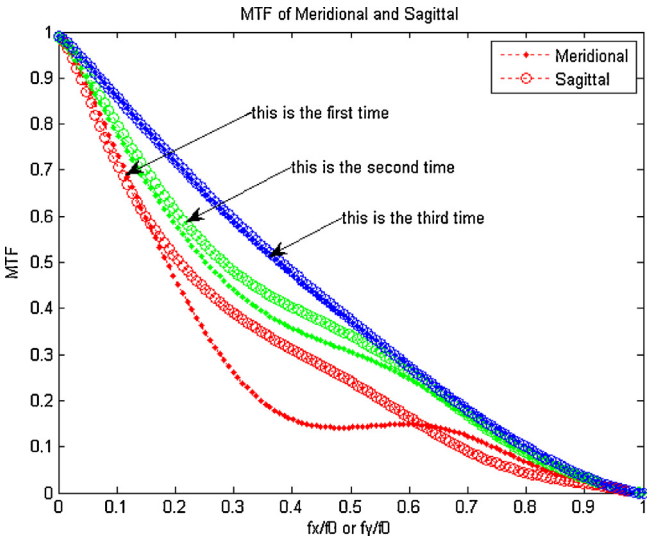

Fig. 7. The estimated MTF of three times.

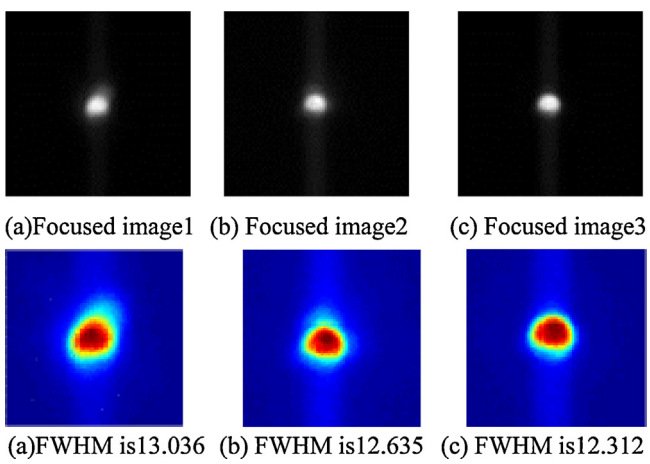

Fig. 8. The comparison of the focus images at each time.

The results of the three experiments are given in Table 1. It shows the normalized Zernike coefficients from fifth term to fifteenth term in the unit of λ. It can be seen that the coefficients value is decreased.

We selected two images from the first five collected images in Fig. 5(a) to resolve the wavefront and recovered the object image. The defocuses of the two channels we selected are 0 mm and 20 mm. The estimated wavefront is displayed in Fig. 9 with $RMS = 0.107\,\lambda$ and $PV = 0.562\,\lambda$. Although the trend of wavefront is

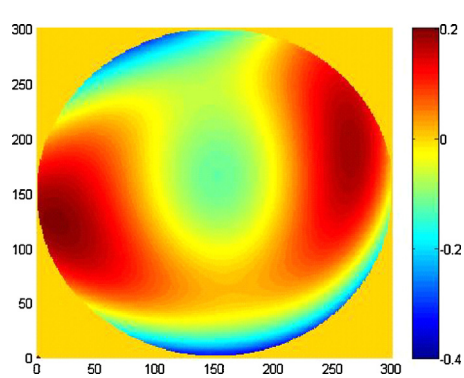

Fig. 9. The wavefront measured by two channels among multi-channel.

Table 2
The comparison of measurement results between double-channel and multi-channel.

Zernike coefficients	Multi-channel	Double-channel
Astigmatism *Y*	−0.04126	−0.04680
Astigmatism *X*	0.07427	0.07289
Coma *Y*	0.03320	−0.02554
Coma *X*	−0.02844	−0.00620
Trefoil *Y*	0.00737	−0.00156
Trefoil *X*	0.009170	−0.01832
Spherical	−0.07451	−0.05148
Secondary astigmatism *Y*	−0.00736	−0.00280
Secondary astigmatism *X*	−0.00041	−0.01127
Tetrafoil *Y*	0.00886	−0.00131
Tetrafoil *X*	0.00095	−0.00379

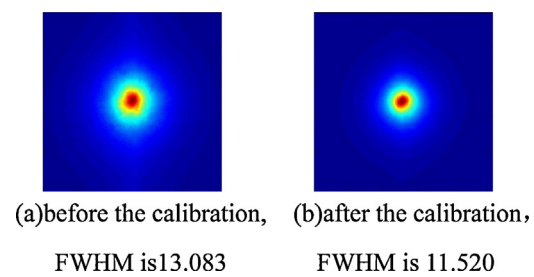

Fig. 10. The image of before and after calibration on Polaris.

similar to that in Fig. 6(a), the aberration of the estimated wavefront is lower. As shown in Table 2, the Zernike coefficients are less than those of result 1 in Table 1. The initialized value of the Zernike wavefront is 0 when PD algorithm initialization. Because the quasi-Newton method is used in the PD calculation algorithm, the algorithm is being trapped into local minima. The local minima are obtained before the Euclidean distance between the points on the value of the *n*-dimensional space. And 0 is often smaller than the Euclidean distance between the point on the value of the wavefront when the global optimal solution consisting of *n*-dimensional space with 0. For the same wavefront, the value of wavefront *RMS* obtained by PD solving the large errors is often smaller than PD solving the small errors.

According to the datum in Table 2, it can be concluded that after the target function transformation, it weakened he wavefront diversity on wavefront constraint solution; thus, the multi-channel PD has higher accuracy than the double-channel PD described in this article.

In order to show that we actually got correction of the mirror shape, we use our method to calibrate the Polaris. When the exposure time is 50 ms, the images that are taken by 100 frames on average collected before and after the calibration of noncommon path aberrations, we can see from Fig. 10, the energy concentration is slightly higher before and after the calibration

5. Conclusion

In this paper, we have designed a system to calibrate the noncommon path aberrations by PD basing on a 137 unit AO system on a 1.23 m telescope. To solve the problems that the defocus cannot be measured and the experimental conditions are nonideal, the tolerance of the measurement conditions of the PD estimation methods was enhanced with improvement of the algorithm. When the measured noncommon path aberrations are compensated, the imaging quality of the telescope image has been remarkably improved. In the future, we will do further research on PD, such as optical estimation and image restoration.

References

[1] M.C. Roggemann, B.M. Welsh, Imaging Through Turbulence, CRC Press, Washington, 1996.
[2] R.A. Gonsalves, Phase retrieval and diversity in adaptive optics, Opt. Eng. 21 (5) (1982) 829–832.
[3] R.G. Paxman, T.J. Schulz, J.R. Fienup, Joint estimation of object and aberrations by using phase diversity, J. Opt. Soc. Am. A 9 (1992) 1072–1085.
[4] R.G. Paxman, J.H. Seldin, M.G. Löfdahl, et al., Evaluation of phase-diversity techniques for solar-image restoration, Astrophys. J. 466 (1996) 1087–1099.
[5] B.J. Thelen, G. Paxman r, D.A. Carrara, et al., Maximum a posteriori estimation of fixed aberrations, dynamic aberrations, and the object from Phase-diverse Speckle data, J. Opt. Soc. Am. A 16 (1999) 1759–1768.
[6] C.R. Vogel, Computational Methods for Inverse Problems, SIAM Press, Philadelphia, PA, 2002.
[7] Vogel C R, Chan T, Plemmons R. Fast algorithms for Phase Diversity-Based Blind Deconvolution [C]. Adaptive Optical System Technologies, *Kona, Hawaii, USA. SPIE*, 3353: 994-1005(1998).
[8] M.G. Löfdahl, T.E. Berger, R.S. Shine, et al., Preparation of a dual wavelength sequence of high-resolution solar photospheric images using phase diversity, Astrophys. J. 495 (1998) 965–972.
[9] Zarifis, V. et al. The Multi Aperture Imaging Array, Working on the Fringe: Optical and IR Interferometry from Ground and Space. Proceedings from ASP Conference Vol. 194. ISBN: 1-58381-020-X (1999).
[10] J. Seldin, et al., Closed-loop wavefront sensing for a sparse-aperture multi telescope array using broadband phase diversity, Proc. SPIE 4091 (2000) 48–63.
[11] Measure Piston Misalignment on the Segmented Primary Mirror of the Keck II Telescope[J], Part of the SPIE Conference on Space Telescopes and Instruments V. Kona, Hawaii March, 3356 (1998) 1190–1201.
[12] A. Blanc, L.M. Mugnier, J. Idier, Marginal estimation of aberrations and image restoration by use of phase diversity, J. Opt. Soc. Am. 20 (6) (2003) 1035–1046.
[13] L.M. Mugnier, et al., On-line long-exposure phase diversity: a powerful tool for sensing quasi-static aberrations of extreme adaptive optics imaging systems, Opt. Express 16 (22) (2008) 18406.
[14] A. Blanc, T. Fusco, M. Hartung, et al., Calibration of NAOS and CONICA static aberrations application of the phase diversity technique, A & A 399 (2003) 373–383.
[15] J.H. Seldin, R.G. Paxman, Phase-diverse speckle reconstruction of solar data – reconstruction and restoration, Proc. SPIE 2302 (1994) 268–280.
[16] J.L. Wang, Z.Y. Wang, B. Wang, et al., Image restoration by phase-diversity speckle, Opt. Precis. Eng. 19 (5) (2011) 1165–1170.
[17] B. Wang, Z.Y. Wang, J.L. Wang, et al., Phase-diverse speckle imaging with two cameras, Opt. Precis. Eng. 19 (6) (2011) 1384–1390.
[18] J.Y. Zhao, Z.F. Chen, B. Wang, et al., Improvement of phase diversity object function's parallelity, Opt. Precis. Eng. 20 (2) (2012) 431–438.
[19] Y.H. Wu, B. Wang, J.Y. Zhao, et al., Restoration of broadband white light image using phase diversity technique, Opt. Precis. Eng. 18 (8) (2010) 1849–1854.
[20] B. Wang, X.X. Ma, et al., Calibration of no-common path aberration in AO system using multi-channel phase-diversity wave-front sensing [J]., Opt. Precis. Eng. 21 (7) (2013) 1683–1692.
[21] N. Accanto, Jana B. Nieder, et al., Phase control of femtosecond pulses on the nanoscale using second harmonic nanoparticles [J], Light Sci. Appl. (2014) 3.
[22] L. Huang, X. Chen, et al., Helicity dependent directional surface plasmon polariton excitation using a metasurface with interfacial phase discontinuity, Light Sci. Appl. (2013) 2.
[23] Richard A. Carreras, Sergio R. Restaino, et al., Phase diversity experimental results: deconvolution of v Scorpii, Opt. Commun. 130 (1996) 13–19.
[24] R.H. Byrd, P. Lu, J. Nocedal, et al., A limited memory algorithm for bound constrained optimization, in: Report NAM-08, EECS Department, Northwestern University, 1994.
[25] C. Zhu, R.H. Byrd, P. Lu, et al., LBFGS-B: Fortran subroutines for large-scale bound constrained optimization, in: Report NAM-11, EECS Department, Northwestern University, 1994.
[26] H. Mahdi, R. Stojan, et al., Memory-enhanced noiseless cross-phase modulation. [J], Light Sci. Appl. (2012) 40.
[27] H. Lingling, C. Xianzhong, et al., Helicity dependent directional surface plasmon polariton excitation using a metasurface with interfacial phase discontinuity [J], Light Sci. Appl. (2013) 2.
[28] D. Dai, J. Bauters, J.E. Bowers, Passive technologies for future large-scale photonic integrated circuits on silicon: polarization handling, light non-reciprocity and loss reduction [J], Light Sci. Appl. (2012) 1.